UC Irvine

Title

Distinguishing Gas-Phase and Nanoparticle Contributions to Small-Angle X-ray Scattering in Reacting Aerosol Flows

Permalink

Journal

ISSN

Authors

Michelsen, Hope A
Campbell, Matthew F
Tran, Ich C
et al.

Publication Date

DOI

Copyright Information

Peer reviewed

Distinguishing Gas-Phase and Nanoparticle Contributions to Small-Angle X-Ray Scattering in Reacting Aerosol Flows

Hope A. Michelsen,[*,†,‡] *Matthew F. Campbell,*[‡,§] *Ich C. Tran,*[⊥,¶] *K. Olof Johansson,*[‡,‖] *Paul E. Schrader,*[‡] *Ray P. Bambha,*[‡] *Joshua A. Hammons,*[⊥] *Eric Schaible,*[○] *Chenhui Zhu,*[○] *and Anthony van Buuren*[⊥]

[†]Department of Mechanical Engineering, University of Colorado Boulder, Boulder, CO 80309 USA

[‡]Combustion Research Facility, Sandia National Laboratories, Livermore, CA 94550 USA

[⊥]Nanoscale Synthesis and Characterization Laboratory, Lawrence Livermore National Laboratory, Livermore, CA 94550 USA

[○]Advanced Light Source, Lawrence Berkeley National Laboratory, Berkeley, CA 94720 USA

[§]Presently at Department of Mechanical Engineering and Applied Mechanics, University of Pennsylvania, Philadelphia, PA 19104 USA

[‖]Presently at KLA Corporation, Milpitas, CA 95035 USA

[¶]Presently at Irvine Materials Research Institute, University of California Irvine, Irvine, CA 92697 USA

*Corresponding author email: Hope.Michelsen@colorado.edu.

Keywords. SAXS, Gas-phase scattering, Nanoparticles, Nucleation, Inception, Soot, Combustion, Flame

ABSTRACT. We have developed a strategy for distinguishing between small-angle X-ray scattering (SAXS) from gas-phase species and newly formed nanoparticles in mixed gas- and particle-phase reacting flows. This methodology explicitly accounts for temperature-dependent scattering from gases. We measured SAXS *in situ* in a sooting linear laminar partially premixed co-flow ethylene/air diffusion flame. The scattering signal demonstrates downward curvature as a function of the momentum transfer (q) at q values of $0.2 - 0.57$ Å^{-1}. The q-dependent curvature is consistent with the Debye equation and the independent-atom model for gas-phase scattering. This behavior can also be modeled using the Guinier approximation and could be characterized as a Guinier knee for gas-phase scattering. The Guinier functional form can be fit to the scattering signal in this q range without *a priori* knowledge of the gas-phase composition, enabling estimation of the gas-phase contribution to the scattering signal while accounting for changes in gas-phase composition and temperature. We coupled the SAXS measurements with *in situ* temperature measurements using coherent anti-Stokes Raman spectroscopy (CARS). This approach to characterizing the gas-phase SAXS signal provides a physical basis for distinguishing the contributions to the scattering signal from the instrument function, flame gases, and nanoparticles. The results are particularly important for analysis of SAXS signal in the q range associated with particles in the size range of $1 - 6$ nm.

1. INTRODUCTION

Pyrolytic and flame-synthesis techniques have become a popular means for producing a wide range of carbonaceous, metallic, and metal oxide nanoparticles.[1-5] However, the inherently high and variable temperatures and chemical reactivity of the synthesis conditions present a challenge for *operando* monitoring and optimization of the synthesis process. Small angle X-ray scattering (SAXS) is potentially extremely useful as an *operando* diagnostic;[2, 5-8] measurements can be performed *in situ* without perturbing the reaction conditions, and the wavelength regime associated with tender to hard X-ray-scattering can provide nanometer-scale spatial resolution for probing particle formation and fine-structure evolution. Such photon energies are also able to penetrate and probe high-pressure systems.

One limitation for the application of SAXS in studies of nucleating particles in reacting flows is the difficulty associated with distinguishing the gas-phase reactants from newly formed particles. The first particles formed from gas-phase reactants, i.e., incipient particles, are in a size range of ~1 nm and are often sparse, and SAXS signals attributable to these particles may be swamped by scattering from reacting gas-phase species. During the first steps of particle formation (i.e., inception), the gas-phase signal can be orders of magnitude larger than that of the particles. The chemical identities of these gases may be unknown and changing, such as in spray-flame synthesis. The problem is exacerbated by the wide range of temperatures (900-2300 K) over which the distinction between gas-phase and particle signals may need to be assessed.

In this paper, we used a sooting diffusion flame as a model for developing a methodology for distinguishing gas-phase from particle-phase signals in *operando* SAXS measurements during nanoparticle formation. In a sooting flame, a hydrocarbon fuel is oxidized and pyrolyzed to form small free radicals and gas-phase hydrocarbon species. These small hydrocarbons and radicals react to form larger gas-phase species, including polycyclic aromatic hydrocarbons (PAHs) and

other precursors to carbon nanoparticle formation. Incipient soot particles are largely composed of PAHs bound together to form small (~1-6 nm) particles.[9, 10] These particles grow and chemically evolve in the flame to form larger particles with complex morphologies.[11, 12] The gas-phase chemical composition and temperature vary throughout the flame and change as the particles form and grow, complicating the distinction between gas-phase and particle signal, particularly during and just after particle inception.

SAXS measurements in a flame involve passing a beam of collimated, monochromatic hard or tender X-ray photons through the flame and measuring the photons scattered by the particles and gas-phase species as a function of scattering angle on a position-sensitive detector placed several meters downstream of the flame. The angular distribution of the scattered photons provides information about the particle-size distribution and morphology.[11, 13]

Although there is a significant body of work describing the use of SAXS to measure particle sizes in flames,[2, 6, 14-33] most of these studies have focused on measuring size distributions of mature particles that have formed aggregates tens of nanometers in size. Previous studies have attempted to isolate the particle signal by making SAXS measurements outside the flame or with the flame turned off[14-19] or at locations in the flame where contributions from particles are assumed to be minimal[20-25] and subtracting this signal from that of the regions of the flame where particle concentrations are significant. This approach removes the instrument function but does not address the temperature and composition-dependent contribution from the flame gases. One approach to estimating the flame-gas component of the SAXS signal is to assume a gas-phase composition and temperature in the flame and calculate the gas-phase scattering.[26, 27] This approach relies on combustion models that can accurately predict the composition and temperature in the flame. For sooting flames, however, reliable chemical kinetic models are not

available. Another approach is to assume a constant (i.e., q-independent) value that varies with height above the burner (HAB), temperature, and composition and is inferred from the high-q signal at each flame location.[28] Alternatively, studies have employed measurements in a relatively lean premixed flame with the same burner configuration as that used for the SAXS soot measurements. The lean-flame measurements are used for background subtraction, assuming that the temperatures and compositions are the same as those in the richer sooting flame.[2, 29-31] Combinations of these approaches can be applied, such as subtracting the signal without the flame or from a non-sooting region of the flame to account for the instrument function, and subtracting a constant, q-independent value determined at high q to account for the temperature effects.[18, 19]

Unfortunately, none of the techniques used previously is suitable for distinguishing between the evolving gas-phase precursors and the newly formed particles. We have developed a methodology to overcome this limitation. Our method explicitly accounts for the temperature- and composition-dependent contributions from gas-phase flame species and isolates them from the instrument function, which is independent of temperature, flame-gas composition, and particle characteristics. We analyzed SAXS data collected along the centerline of a sooting, partially premixed, ethylene-air diffusion flame, which was studied previously using coherent anti-Stokes Raman spectroscopy (CARS).[34] We combined CARS temperature measurements with SAXS measurements to distinguish between the temperature-independent instrument function and the temperature-dependent gas-phase signal. The temperature measurements also allowed us to fit the gas-phase signal to gain some information about its evolution in the flame. Our results consistently demonstrated a gas-phase Guinier knee at values in the momentum transfer (q) range of 0.2-0.57 Å^{-1}. We fit this feature in this q range, accounting for temperature,

to provide an estimate of the gas-phase signal in the absence of knowledge of the gas-phase composition at each HAB.

Section 2 provides information about the experimental methodology. Section 3.1 presents a method for extending the utility of the Guinier functional form to higher values of q, enabling its use for fitting gas-phase SAXS signal. Section 3.2 shows that, at constant q, scattering from gases is inversely proportional to temperature. Section 3.3 exploits the temperature dependence of the gas-phase signal to distinguish the gas-phase signal from the instrument function in the absence of particles. Section 3.4 demonstrates the use of the Guinier exponential form factor to fit the gas-phase signal from the sooting flame. Section 3.5 presents the retrieval of the soot signal from the total normalized signal in the sooting flame. Section 4 provides a summary of the paper and general conclusions.

2. EXPERIMENT

We performed SAXS experiments in a sooting linear ethylene/air coflow diffusion flame at Beamline 7.3.3 at the Advanced Light Source (ALS) at Lawrence Berkeley National Laboratory.[35] We made these measurements on the flame centerline as a function of height above the burner (HAB). We conducted similar experiments in a hydrogen/air coflow diffusion flame using the same burner as a non-sooting reference case. No unexpected or unusually high safety hazards were encountered.

2.1 Beamline Setup

Details regarding the setup of Beamline 7.3.3 at the ALS are available in a paper by Hexemer *et al.*,[35] and only a brief description will be provided here. The beamline employs a multilayer monochromator with an energy resolution of $\frac{\Delta E}{E} = 0.01$ to provide 10-keV (1.24-Å) X-ray

photons at a flux of ~1.3×10^{12} photons/s. A toroidal mirror focuses the beam to a size of ~500×400 μm^2 (*W*×*H*) at the measurement location. The beam is approximately 90% horizontally polarized. The beam passes from the beamline vacuum system to the ambient-pressure room air through a 100-μm-thick muscovite mica window. The beam has a slight downward angle (0.5-degrees), yielding, together with the beam size, a vertical position uncertainty of ±~370 μm in our flames.

After exiting the vacuum tube, the photons travel through an ion chamber that monitors the incident beam intensity (see Fig. 1). X-ray scattering caused by the room air originating near the mica window is captured using a 1.5-mm diameter pinhole located close to the burner at the end of a 90-mm long aluminum tube. Upon exiting this beam tube, the photons travel through a 7-mm air gap and then pass through the flame. The burner (described below) is mounted on a remotely controlled stage and can be translated vertically and horizontally relative to the X-ray beam.
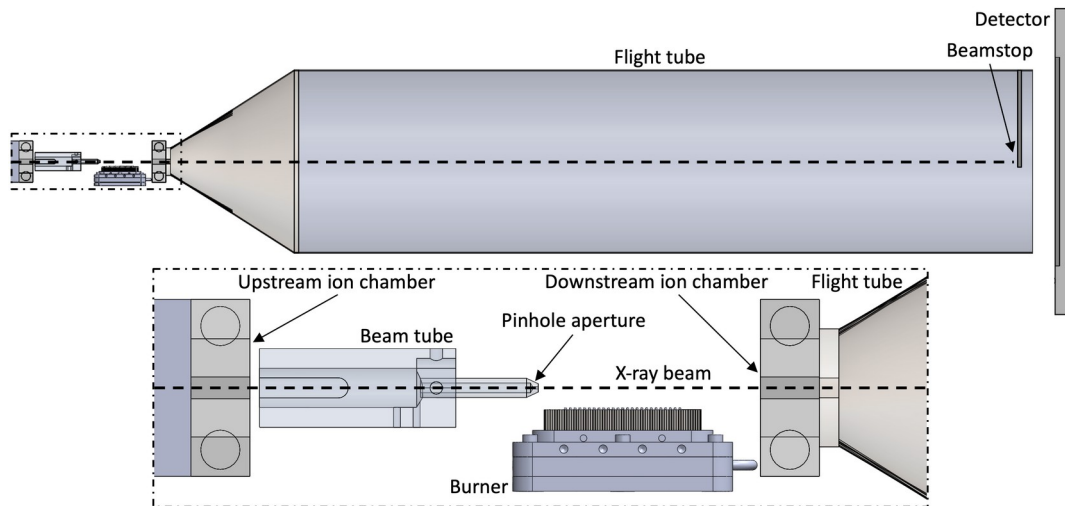

Figure 1. Beamline and burner geometry. The flame region outlined by the dot-dashed rectangle in the top part of the figure is enlarged and displayed in the bottom portion of the figure.

On the downstream side of the flame, the scattered photons and collimated beam pass through another air gap (26 mm) and a second ion chamber and enter an evacuated flight tube through a Kapton polyimide film (DuPont) window. At the end of the flight tube, the radiation exits through a second Kapton film followed by a small (~25 mm) air gap, and the scattered photons are detected by a two-dimensional single-photon counting detector (Dectris Ltd. model Pilatus 2M). The distance between the center of the flame and the detector in this work was $d = 1314$ mm. A beam stop is used to prevent the incident beam from reaching the detector, and a diode on this beam stop provides a second monitor of the intensity of the X-ray beam.[36] Typically the beam intensity downstream of the sample would be measured using the second ion chamber, but the flame caused significant perturbations to the ion-chamber signal. This type of perturbation to the ion-chamber signal from a flame was observed by England[14] in the first SAXS measurements made in a flame. We thus used the signal on the beam-stop diode as a measure of the downstream beam intensity. The radius of the beam stop r_{min} and the half-width of the detector r_{max} dictate the minimum and maximum observable scattering angles θ_{min} and θ_{max}, respectively. The q range for these measurements was approximately 0.017 - 0.57 Å^{-1}, and exposure times were 300 seconds for each position in the flame.

2.2 Burner and Flames

In these experiments, we used a novel linear Hencken-type burner geometry, which produces long, narrow partially-premixed laminar co-flow diffusion flames, as shown in Fig. 2.[34] Briefly, the burner consists of a 25×50 mm^2 [W×L] hexagonal mesh, in the center of which is a line of 25 small-gauge fuel tubes (each with an inside diameter of 508 μm). Dry, hydrocarbon-free air flows through the hexagonal mesh, and fuel (neat ethylene or hydrogen/nitrogen mixtures) flows

through the small-gauge tubes. This geometry produces a flame that is ~3 mm wide and ~38 mm long, providing a significant distance along the long axis for soot-photon interactions. Scattering occurring at the front and rear of the flame produces some uncertainty in the exact scattering length (d_{cm} = 131.4±1.9 cm), resulting in a small uncertainty in q of $\frac{\Delta q}{q} \leq \pm 1.5\%$. In addition, the flame length changes with height above the burner, the effects of which are discussed in Section 3.3 below.
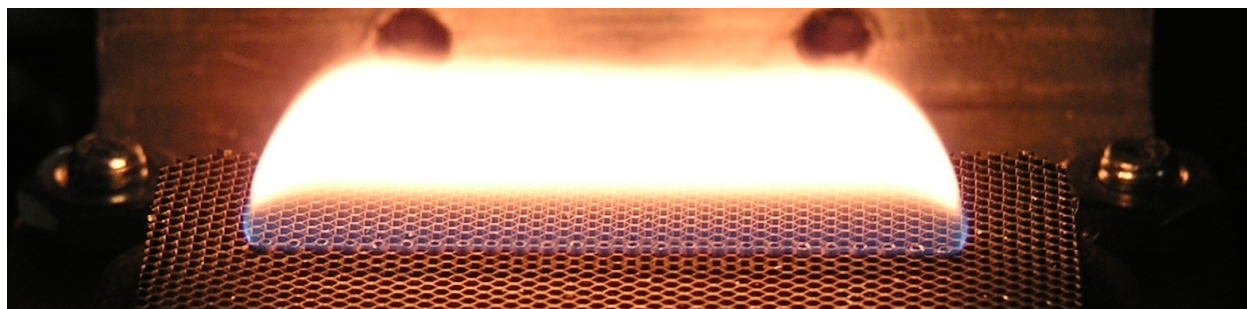

Figure 2. Photograph of Flame E1.

Table 1 provides gas flow rates in standard (0 °C, 1 atm) liters per minute (SLM) for the flames examined in this work (henceforth, these flames will be referred to by the descriptors in this table). Mass flow controllers (MKS Instruments, Inc. Model GM50A) were used to ensure flow stability (±3% at full scale) and were calibrated (using a Sierra Instruments, Inc. Model SL-500) prior to use. Research-grade gases were supplied by Airgas, Inc. and were filtered (Swagelok Model SS-4F-05) immediately upstream of the mass flow controllers. House air was dried (Parker Hannifin Corp. Model IT0030-35) and passed through a carbon filter (Parker Hannifin Corp. Model 2002N-0A0-000/CI100-12-000) to remove hydrocarbons prior to entering its mass flow controller. In the hydrogen/nitrogen flame, a bladed tube (McMaster-Carr Supply Co. Model 3529K51) was used to ensure adequate hydrogen/nitrogen gas mixing. A chiller

(NESLAB Instruments, Inc. Model RTE-111) supplied cool distilled water to the burner to maintain a burner temperature of ~20°C. The burner itself was mounted inside an acrylic flame enclosure to capture exhaust and prevent flame fluctuations produced by room-air currents; this enclosure attached to the beamline's remotely controlled *X-Z* stage, which allowed a range of locations in the combustion environment to be probed with the incident X-ray beam.

This manuscript presents the analysis of three datasets for the ethylene flame (E1a, E1b, and E1c) and two datasets for the hydrogen flame (H1a and H1b). In each dataset the burner was translated vertically, and SAXS data were collected at selected heights in the burner along the centerline of the flame. For E1c, data were taken at HABs in the range of 2-11.5 mm, and, for all other datasets, data were taken between 2 and 20 mm.

Table 1. Flow Rates for Flames E1 and H1

Flame	C_2H_4 (SLM)	H_2 (SLM)	N_2 (SLM)	Air (SLM)	Fuel mix velocity (cm/s)	Air velocity (cm/s)
E1	0.200	N/A	N/A	14.0	65.8	22.0
H1	N/A	1.30	1.30	14.0	855.2	22.0

We measured flame temperatures on the flame centerline using coherent anti-Stokes Raman spectroscopy (CARS) on Flames E1 and H1 and soot volume fractions using laser-induced incandescence (LII) on Flame E1, details of which are reported elsewhere.[34] These results are displayed in Fig. 3. The gas temperature in both flames (Fig. 3a) initially increases with increasing height above burner (HAB) because of combustion-energy release, and then decreases slowly at locations well above the luminous flame region. The mature-soot volume fraction increases dramatically in the lower part of the flame as soot is formed and matures at temperatures above ~1700 K; the volume fraction decreases higher in the flame as soot is

oxidized. As shown in Fig. 3b, regions at HABs below ~3 mm and above ~11 mm do not have measurable mature soot.
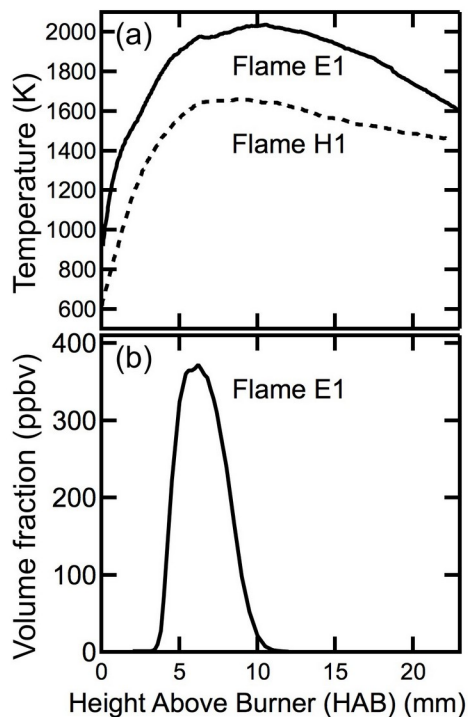

Figure 3. Flame temperatures and soot-volume fractions. (a) Temperatures were measured using CARS along the flame centerline of the ethylene flame (Flame E1, solid line) and the hydrogen flame (Flame H1, dotted line). (b) Soot-volume fractions were measured using LII along the flame centerline of the ethylene flame (Flame E1). There data were published previously and described in detail by Campbell *et al.*[34]

2.3 Beam-Flame Interaction Pathlength. As in other linear-type flames,[37, 38] the pathlength for X-ray/soot interactions in our burner decreases with increasing height above the burner (HAB). In Flame E1, the flame length is nearly constant up to ~3 mm above the burner, at which point it begins to decrease; its minimum length at its highest distance from the burner is approximately 32% less than its maximum of about 38 mm. Combustion occurs at the ends of

11

the linear flame generated by this burner and not just on its long edges. A discussion of the influence of end flames is provided by Miller *et al.*[39] In our case, we anticipate that the influence of end flames is approximately constant with increasing HAB. Neglecting the influence of the end flames, the total scattering length is anticipated to modify the overall intensity of the scattering information rather than its angular distribution. Thus, to a first approximation, the particle sizes and morphological information derived from the analysis are independent of the flame length.

2.4 Azimuthal Averaging. We performed azimuthal averaging on the two-dimensional (2D) scattering images from the detector using the Nika software (Release 1.74)[40], which is a set of Igor Pro (Version 6.37, WaveMetrics)[41] macros that calibrate and reduce 2D images to 1D profiles of integrated intensity *vs. q*. The Nika software package[40] provides the standard deviation of the mean in the azimuthally-averaged signal during the 2D-to-1D conversion process. We corrected these 1D profiles for variations in the incident photon flux and transmittance of the flame and background gas, described in more detail below.

3. RESULTS AND DISCUSSION

3.1 Molecular Form Factors and Composition Effects for Gas-Phase Scattering. The scattering efficiency (i.e., the scattering intensity normalized by the beam intensity) for a dilute gas $I_{gas}(q)$ can be approximated as[42]

$$I_{gas}\left(q > \frac{2\pi}{D_{scat}}\right) = I_e(q) V_{scat} \acute{N}_{gas} F_m(q), \tag{1}$$

where D_{scat} is the average dimension of the detection volume (2.0×10^7 Å in our case); V_{scat} is the detection volume (7.6×10^{-3} cm^3 in our case); $\acute{N}_{gas}$ is the average gas number density; $I_e(q)$ is the scattering efficiency for a single electron, and $F_m(q)$ is the molecular form factor. Because of

uncertainties introduced by averaging over a discrete sample size, Eqn. (1) is estimated to be valid for q values greater than $2\pi/D_{scat}$, i.e., $q > 3.2\times10^{-7}$ Å^{-1}, based on the dimensions of our X-ray beam. The classical, elastic scattering efficiency of a single electron is given by[42, 43]

$$I_e(q)=r_0^2 d_{cm}^{-2} P_\psi ,$$
(2)

where d_{cm} is the distance to the detector in cm. The momentum transfer q is given by

$$q=\frac{4\pi}{\lambda}\sin\left(\frac{\theta}{2}\right)=\frac{2\pi}{L} ,$$
(3)

where λ is the wavelength of incident photons (1.24 Å). The angle between the X-ray beam and the trajectory of the scattered photon is given by $\theta=\tan^{-1}\left(\frac{r}{d}\right)$ for a photon hitting the detector a distance r from the X-ray beam with a distance d between the center of the flame and the detector beam stop. L is the characteristic size of particles scattered at angle θ.[17, 18] In our experiments, the range of q was approximately 0.017 - 0.57 Å^{-1}. The polarization correction term is expressed as

$$P_\psi=\pi\left(1+\cos^2\theta\right)$$
(4)

for an azimuthally averaged scattering signal with horizontally polarized radiation.[44] The Thomson scattering length (or classical Thomson electron radius)[45] is given by $r_0=\frac{e^2}{mc^2}$,[46] where e is the charge of an electron (1.602177×10^{-19} C); m is the mass of an electron (9.1093836×10^{-28} g), and c is the speed of light (2.9979246×10^{10} cm/s), such that $r_0=2.81794\times10^{-13}$ cm. The square of the Thomson scattering length gives the differential Thomson cross section for a free electron,[43] i.e., $r_0^2=7.94079\times10^{-26}$ cm^2.

The molecular form factor in Eq. (1) can be approximated according to the method proposed by Debye,[43, 47, 48] i.e.,

$$F_{m,\text{Debye}}(q)=\sum_{\alpha=1}^{N_{at}}\left[|f_{\alpha}(q)|^{2}+S_{\alpha}(q)+\sum_{\beta=1;\beta\neq\alpha}^{N_{at}}f_{\alpha}(q)f_{\beta}(q)\frac{\sin\left(qr_{\alpha\beta}\right)}{qr_{\alpha\beta}}\right]$$

(5)

where α and β represent individual atoms; $r_{\alpha\beta}$ is the distance between them, and N_{at} is the number of atoms in the molecule; $f_{\alpha}(q)$ and $f_{\beta}(q)$ are atomic form factors, and $S_{\alpha}(q)$ is the incoherent (i.e., Compton) atomic scattering term. The atomic form factors can be represented using the following functional form[49]

$$f_{\alpha}(q)=\sum_{i=1}^{4}\left[a_{i}e^{-b_{i}\left(\frac{q}{4\pi}\right)^{2}}+c\right]$$

(6)

for which the coefficients are provided in Table 6.1.1.4 of the International Tables of Crystallography.[49] These coefficients provide a close representation of calculated atomic scattering curves for $0 < q < 25$ Å^{-1}.[49] The coefficients used in our analysis are given in Table S1 in the Section B of the supplementary material. We used values of $S_{\alpha}(q)$ tabulated by Hubbell et al.[50, 51] and values of $r_{\alpha\beta}$ calculated using equilibrium molecular structures and atom positions optimized using Avogadro (Version 1.2.0).

Calculating the gas-phase signal using Eq. (1) with the molecular form factors given by the Debye equation would require an estimate of the chemical composition of the flame gases and a summation of the scattering from all chemical species at every measurement position. These calculations would, in turn, require predictions of reactive-gas composition and temperature using a chemical kinetic model. In many cases, such a model does not exist, as is the case for rich sooting flames.

Alternatively, the molecular form factor can be expressed according to the Guinier exponential function according to[42]

$$F_{m,\text{Guinier}}\left(q<\frac{1.3}{R_e}\right)=n_e^2\exp\left(\frac{-q^2R_e^2}{3}\right),\tag{7}$$

where n_e is the number of electrons per molecule of a gas-phase species, and R_e is the electronic radius of gyration for that species. To a first approximation, values of R_e can be calculated according to

$$R_e=\left\{\frac{1}{n_e}\sum_{a=1}^{N_{at}}n_{e,a}\left[(x_a-x_{Ce})^2+(y_a-y_{Ce})^2+(z_a-z_{Ce})^2\right]\right\}^{\frac{1}{2}}\tag{8}$$

where $n_{e,a}$ is the number of electrons for atom α; x_α, y_α, and z_α are the coordinates for atom α, and x_{Ce}, y_{Ce}, and z_{Ce} are the coordinates for the center of electron density in that molecular species, e.g.,

$$x_{Ce}=\frac{1}{n_e}\sum_{a=1}^{N_{at}}n_{e,a}x_a\tag{9}$$

Molecular form factors given by Eq. (7) are valid for q values less than $1.3/R_e$.[52, 53] Molecular species with $R_e > 2.4$ Å are within the limit of validity of the Guinier approximation for our experiment. Some hydrocarbon species are within this limit, as shown by the values of R_e calculated using Eq. (8) and presented in Table S2 in Section B of the supplementary material, but the smaller species are outside this range.

Figure 4 shows a comparison of molecular form factors calculated using the Guinier approximation, Eq. (7), and the Debye equation, Eq. (5), for carbon monoxide (CO), ethylene (C_2H_4), and pyrene ($C_{16}H_{10}$). The differences between the Guinier and Debye form factors are large for CO ($R_e = 0.558$ Å) and ethylene ($R_e = 0.959$ Å) but are much smaller for pyrene ($R_e = 2.703$ Å); pyrene falls within the validity limits of the Guinier approximation for our q range of $q \leq 0.57$ Å^{-1}, but CO and ethylene are too small to be within these validity limits.
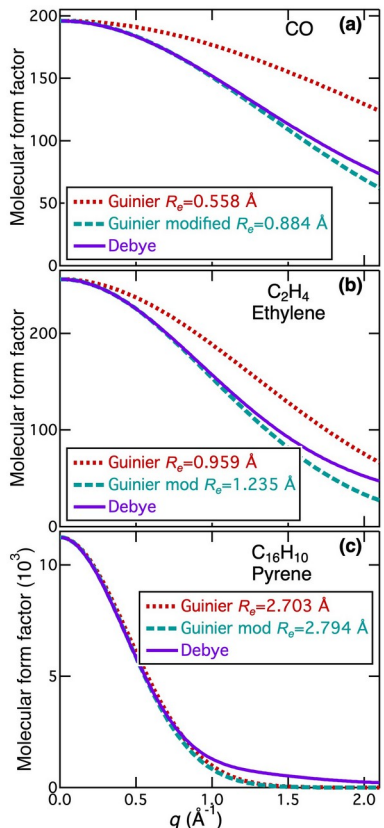
Figure 4. Molecular form factors for gas-phase species. The q dependence of molecular form factors is shown for (a) carbon monoxide, (b) ethylene, and (c) pyrene. Molecular form factors were calculated using the Debye equation, Eq. (5), and the Guinier approximation, Eq. (7). The calculations for the Guinier approximation were performed using Eq. (8) to calculate R_e or using modified values of R_e, the latter of which provide agreement with the Debye equation at $q < \sim 1.0$ Å^{-1}.

We can, however, achieve excellent agreement between the Guinier and Debye molecular form factors for all species for $q < \sim 1$ Å^{-1} by using slightly larger values of R_e in the Guinier calculation. An increase in R_e suggests a larger effective range in electron density than predicted by the simple calculation in which the electrons are assumed to reside at the equilibrium positions of the atoms, i.e., Eq. (8). This result is consistent with electron densities of the

molecular orbitals extending beyond the atom locations. When modified values of R_e are used, the Guinier form factors and the Debye form factors are nearly indistinguishable for $q \leq 0.57$ Å^{-1}, as shown in Fig. 4. Even for the smallest species, e.g., CO and C_2H_2, the modified Guinier form factors are larger than the Debye form factors by only 5-6%; at a q of 1 Å^{-1}, modified Guinier form factors are <20% larger.

For species with $R_e > 2.4$ Å, which corresponds to $n_e > 82$, the values of R_e modified to bring the Guinier form factors into agreement with the Debye form factors are only 1-3% larger than the values of R_e calculated using Eq. (8). The differences between the original and modified values of R_e increase with decreasing size. Comparisons of the values calculated using Eq. (8) with the modified values are shown in Fig. 5. Table S2 in Section B of the supplementary material lists R_e and the modified values shown in Fig. 5. This result extends the usefulness of the Guinier functional form to higher values of q so that it can be used for the form factor in Eq. (1) for gas-phase scattering. The Guinier functional form is much easier to use in fits to the data than the Debye function. To facilitate the analysis further, we fit the modified values of R_e as a function of n_e, as shown in Fig. 5. The fit is given by

$$R_{e,\,\text{Modified}} = (0.646 \pm 0.051) + (0.0290 \pm 0.0015)\,n_e - (0.0000667 \pm 0.0000082)\,n_e^2. \quad (10)$$
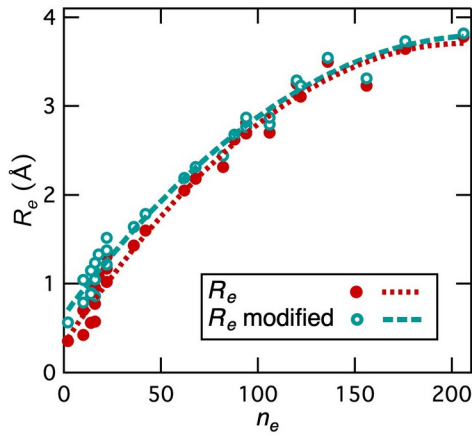
Figure 5. Electronic radius of gyration versus number of electrons for gas-phase species. R_e is plotted as a function of n_e for selected species. Closed symbols represent values calculated using Eq. (8) and given in Table S2. The dotted line is a fit to these values. The open symbols show values modified to provide agreement with the calculations using the Debye form factors. The dashed line is a fit to these values.

3.2 Temperature Effects for Gas-Phase Scattering in Non-Sooting Regions. Using the ideal-gas equation of state, we can rewrite Eq. (1) as

$$I_{gas}(q) = I_e(q) V_{scat} \frac{P_{atm}}{k T_{gas}} F_m(q) = \frac{A_{gas}(q)}{T_{gas}} , \qquad (11)$$

where P_{atm} is the ambient pressure; k is the Boltzmann constant (1.3626×10^{-22} atm cm^3/K), and T_{gas} is the gas temperature. The parameter $A_{gas}(q)$ has units of K and is independent of temperature but depends on the gas composition and q, i.e.,

$$A_{gas}(q) = r_0^2 d_{cm}^{-2} P_{\psi} V_{scat} \frac{P_{atm}}{k} F_m(q) , \qquad (12)$$

where P_{ψ} is given in Eq. (4) with $\theta = 2 \sin^{-1} \frac{\lambda q}{4\pi}$.

The normalized raw scattering signal from a non-sooting flame or sootless region of a sooting flame can be expressed as

$$\frac{S_{nsraw}(q)}{\psi_{ns1}} = C \frac{A_{nsgas}(q)}{T_{nsgas}} + C I_{inst}(q) , \qquad (13)$$

where $S_{nsraw}(q)$ is the raw scattering signal and ψ_{ns1} is the signal from the detector downstream of the sootless region (see Section A of the supplementary materials for more information about signal normalization); $A_{nsgas}(q)$ is a parameter that varies with gas composition, and T_{nsgas} is the flame temperature, both of which vary with HAB, and C is the instrument calibration factor. Figure 6 shows the normalized signal for Flame H1 (non-sooting flame), compared with signal from the sootless regions of Flame E1 (sooting flame) at low and high HABs. The peak at q of

0.37 Å^{-1} is an interference from the Kapton window at the entrance to the flight tube. Normalized signal profiles are available in the supplementary material.
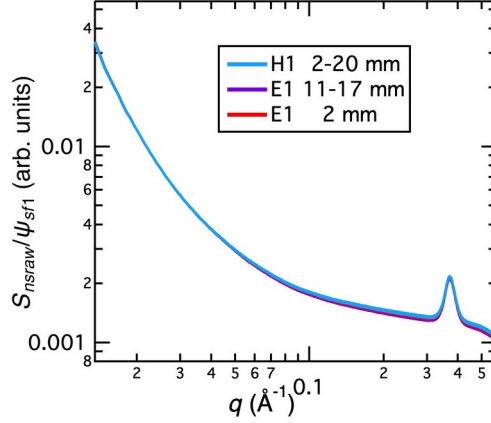

Figure 6. Normalized scattering signal for a range of HABs. The total normalized signal is shown as a function of q for HABs between 2 mm and 17 mm for Flame H1a. Flame H1a signal is compared with signal from Flame E1b in the non-sooting regions (see legend).

Because C is independent of HAB, we can subtract the scattering profile at one HAB (HAB0) from each of the others (HABx), yielding

$$\frac{S_{nsraw}(q, \mathrm{HAB}\,x)}{\psi_{ns1}} - \frac{S_{nsraw}(q, \mathrm{HAB}\,0)}{\psi_{ns1}} = C\left[\frac{A_{nsgas}(q, \mathrm{HAB}\,x)}{T_{HABx}} - \frac{A_{nsgas}(q, \mathrm{HAB}\,0)}{T_{HAB0}}\right], \qquad (14)$$

where T_{HABx} is the temperature of the gas at HABx. Plotting this difference at a single value of q as a function of $1/T_{HABx}$ and fitting it to a line will yield a slope of CA_{nsgas} and an intercept of $-CA_{nsgas}(\mathrm{HAB}0)/T_{HAB0}$ at that q value.

Figure 7 shows examples of plots of the differenced scattering signal for all HABs as a function of the inverse temperature at several values of q. The value of HAB0 is 2 mm. Results are shown in Fig. S2 in the supplementary material for an HAB0 of 8 mm for Flame H1 and 11 mm for Flame E1. Points represent different HABs for HABx, a few of which are indicated in the figure. Both temperature and composition vary with HAB. These plots show regions in the

flames with a linear dependence on $1/T_{nsgas}$; these linear regions indicate ranges in HAB over which the temperature dependence dominates over the gas-phase-composition dependence in determining the change in scattering signal with HAB. For our hydrogen flame diluted with nitrogen, at HABs of 8 mm and above, the composition is predominantly H_2O and N_2, which includes some gas mixing from the air co-flow of the burner. In the ethylene flame, the volume fraction of mature soot (i.e., refractory, turbostratic-graphite particles) at 11 mm and above is $\leq$ 0.7% of its peak value (measurements of mature soot using laser-induced incandescence are shown in Fig. 3b in the supplementary material),[34] and the gas composition is predominantly CO_2, H_2O, and N_2, including some co-flow air mixing.
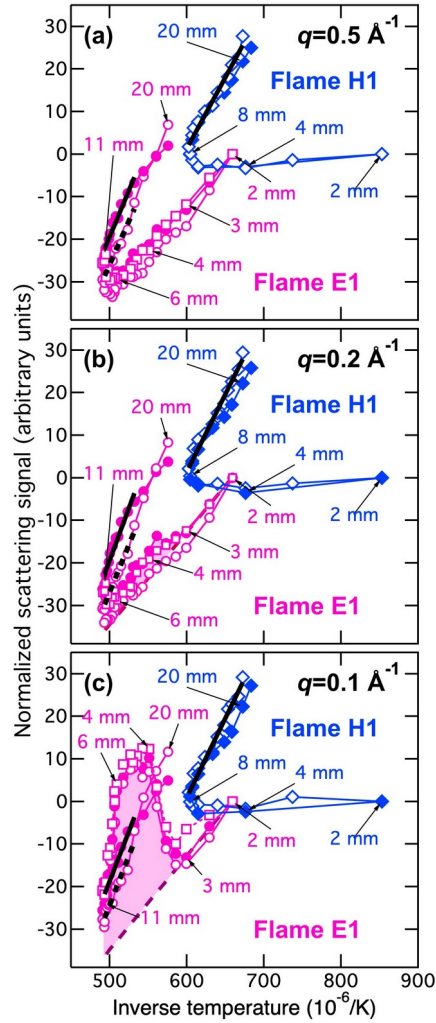
Figure 7. Differenced scattering signal versus inverse temperature at selected values of *q*. Symbols indicate the difference between the signal at each HAB and the signal at one selected HAB in the non-sooting region of the flame (HAB0 = 2 mm). These values are plotted for Flames H1 (blue) and E1 (magenta) as a function of $1/T_{HABx}$ at values of *q* of (a) 0.5 $\mathring{A}^{-1}$, (b) 0.2 $\mathring{A}^{-1}$, and (c) 0.1 $\mathring{A}^{-1}$. Different symbols represent different datasets. Lines show fits to the high HABs for Flame H1 between 8 and 20 mm and for Flame E1 between 11 and 17 mm, inclusive. Selected HABs are indicated in the figure.

For the hydrogen flame at all values of *q*, the plots show a linear decrease in scattering with increasing HAB at low HABs and a linear increase in scattering with increasing HAB at high

HABs. The same behavior is observed at $q = 0.5$ Å^{-1} for the ethylene flame (Fig. 7a) and at high

HABs at all values of q for this flame and is related to the temperature dependence of the

scattering in the absence of a strong soot signal. At values of q where soot is prominent, a peak

appears at HABs between 3 and 11 mm, an example of which is shown by the shaded region for

the ethylene flame in Figs. 7b and 7c. The dashed red line in Figs. 7b and 7c represents the

extrapolated linear fit to the data from HABs of 2-3 mm for Flame E1b, as is seen in the absence

of soot, and the shaded region shows the deviation from that relationship attributable to soot

scattering. This signal increases with decreasing q because scattering from soot is substantial for

larger particles observable at lower q values. The shaded regions indicate scattering from

incipient particles with a size scale on the order of ~3 nm in Fig. 7b and ~6 nm in Fig. 7c.

The lines in Fig. 7 show fits to the non-sooting regions of Flame E1 and the linear region of

Flame H1 at high HABs. The associated slopes, i.e., CA_{nsgas}, are shown as symbols in Fig. 8 for

differenced signals in which HAB0 was 2 mm. Figures S2 and S3 in the supplementary material

show results of the same analysis for HAB0 of 8 mm for Flame H1 and 11 mm for Flame E1.
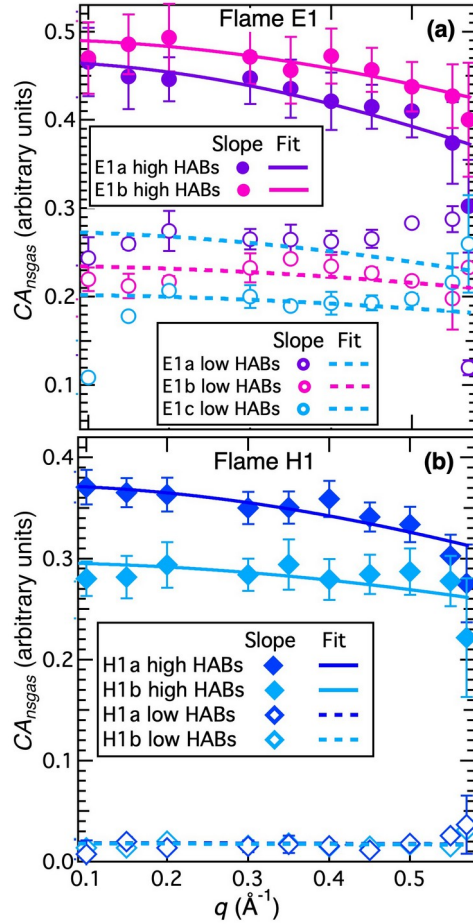
Figure 8. Inferred values of CA_{nsgas}. Symbols represent results of linear fits to the differenced scattering signal versus $1/T_{HABx}$ for (a) Flame E1 and (b) Flame H1. Solid symbols show results for high HABs; open symbols, for low HABs. The error bars represent 1-σ uncertainties derived from the fits. Fits of the differenced scattering signal were performed in the HAB ranges (inclusive) of 11-17 mm and 2-3 mm for Flame E1 and 8-20 mm and 2-4 mm for Flame H1. The lines represent results of weighted fits to values of CA_{nsgas} using Eq. (12), multiplied by the scaling factor C, with $F_m(q)$ represented by Eq. (7) and R_e given by Eq. (10). Fits to the data were performed over the q range of 0.10-0.57 Å^{-1} with C and n_e as adjustable parameters.

At values of q of 0.08-0.2 Å^{-1}, the slopes are nearly independent of q. At values of q smaller than 0.08 Å^{-1}, the scattering profiles are less sensitive to the gas-phase component, and the slopes

defined by the dependence of the scattering profiles on the gas-phase temperatures are difficult to extract from the data. At values of q greater than 0.1 Å^{-1}, there is a statistically significant decrease in CA_{nsgas} with increasing q. Such behavior was observed previously in an X-ray scattering study of soot in flames[27] and is consistent with predictions of gas-phase scattering using the independent-atom model to calculate molecular form factors.[43] The drop in signal at these values of q could be described as a "Guinier knee" for gas-phase scattering. Our observations of this behavior at high temperatures and atmospheric pressure are enabled by our ability to isolate the temperature-dependent gas-phase signal from the much larger temperature-independent background. Provided we account for this change in gas-phase scattering, the decrease in gas-phase scattering in this range of q values favors detection of incipient particles.

3.3 Temperature and Composition Effects for Gas-Phase Scattering in Non-Sooting Regions. The lines in Fig. 8 show weighted fits to the q dependence of CA_{nsgas} derived from the slopes, using Eq. (12) to represent $A_{nsgas}(q)$ and Eq. (7) to represent $F_m(q)$, weighted by the instrument calibration factor C, i.e.,

$$C I_{gas}(q) = C \frac{A_{gas}(q, \text{HAB } x)}{T_{gas}(\text{HAB } x)} = C r_0^2 d_{cm}^{-2} P_\psi V_{scat} \frac{P_{atm}}{k T_{gas}(\text{HAB } x)} n_e^2 \exp\left(\frac{-q^2 R_e^2}{3}\right). \tag{15}$$

We used Eq. (10) to represent the modified values of R_e (Å) as a function of n_e (dashed line in Fig. 5). The fits to the slopes shown in Fig. 8 were performed with C and n_e as adjustable parameters over the q range of 0.10-0.57 Å^{-1}, assuming d_{cm} = 131.4 cm, V_{scat} = 0.05 cm $\times$ 0.04 cm $\times$ 3.8 cm, λ = 1.2398 Å, and P_{atm} = 1 atm. In the fits to the low HAB slopes, values of C were constrained to those derived from fits to the high HAB slopes, except for Flame E1c for which there were no high HAB measurements. The values resulting from these fits are given in Table S3 in Section B of the supplementary material. Results are given for the analysis in which HAB0

was 2 mm in the third and fourth columns and in which HAB0 was 11 mm for the ethylene flame and 8 mm for the hydrogen flame in the fifth and sixth columns. Results of the analyses with different values of HAB0 demonstrate excellent agreement.

The results suggest that, for the ethylene flame, the molecular species have an average number of electrons of 22.9 ± 8.0 high in the flame and 15.0 ± 6.0 low in the flame. These ranges are consistent with species expected at low HABs [e.g., C_2H_4 (n_e=16), O_2 (n_e=16), and N_2 (n_e=14)] and at high HABs [e.g., CO_2 (n_e=22), H_2O (n_e=10), and N_2 (n_e=14)]. For the hydrogen flame, the average values of n_e are 18.0 ± 5.4 high in the flame and 4.2 ± 1.0 low in the flame; within the experimental uncertainties, these values are also consistent with species expected high in the flame [e.g., H_2O (n_e=10) and N_2 (n_e=14)] and low in the flame [e.g., H_2 (n_e=2), N_2 (n_e=14), O_2 (n_e=16), and H_2O (n_e=10)].

3.4 Temperature and Composition Effects for Gas-Phase Scattering in Sooting Regions. Subtracting the scattering profile at HAB0 from the signal at HABs in sooting regions and rearranging yields

$$C\frac{A_{sfgas}(q,\text{HAB}\,x)}{T_{sfgas}(\text{HAB}\,x)}+CI_{soot}(q,\text{HAB}\,x)=\frac{S_{sfraw}(q,\text{HAB}\,x)}{\psi_{sf\,1}}-\frac{S_{nsraw}(q,\text{HAB}\,0)}{\psi_{ns\,1}}+C\frac{A_{nsgas}(q,\text{HAB}\,0)}{T_{nsgas}(\text{HAB}\,0)}.$$
(16)

Figure 9 shows examples of the normalized signal from the sooting flame, the first two terms on the right-hand side of Eq. (16). The last term on the right-hand side of Eq. (16) was determined in the analysis presented in Section 3.3 from the fits to the data shown in Fig. 8.
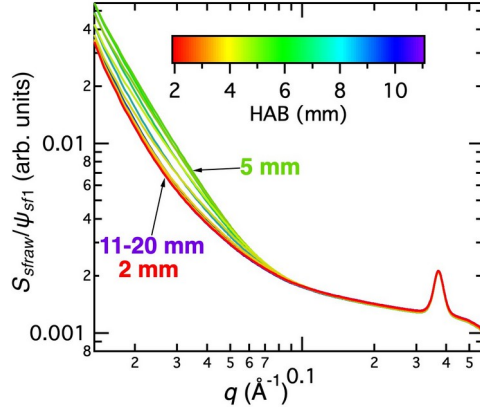
Figure 9. Normalized scattering signal for a range of HABs. The total normalized signal is shown as a function of q for HABs between 2 mm and 17 mm for Flame E1b. Lines are color coded by HAB as indicated by the color scale.

Figure 10 shows the sum of the terms on the right-hand side of Eq. (16). In Fig. 10, the signal at high q is expected to be predominantly attributable to gas-phase scattering. To determine

$C \dfrac{A_{sfgas}(q, \text{HAB } x)}{T_{sfgas}(\text{HAB } x)}$, the first term on the left-hand side of Eq. (16), we fit the data in Fig. 10 using Eq. (15) for each HAB in the q range of 0.2-0.57 Å^{-1}, assuming negligible contribution from soot. C was constrained to values derived in fits to the slope and intercept shown in Fig. 8 (given in Table S3), and n_e and R_e were adjustable parameters.
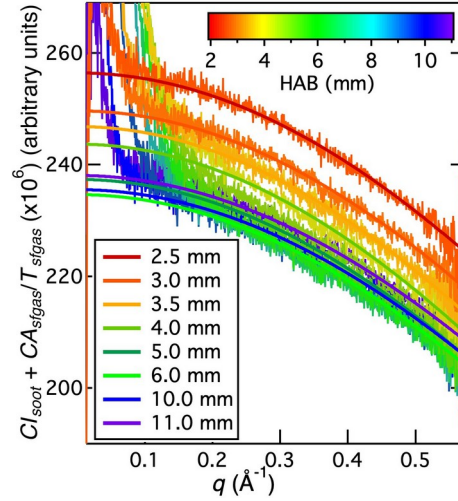
Figure 10. Fits to the gas-phase contribution to the scattering signal. Colored lines represent the sum of the terms on the right-hand side of Eq. (16). The smooth lines show the results of fits to the data for selected HABs over a q range of 0.2-0.57 Å^{-1} to yield estimates for the value of the first term on the left-hand side of Eq. (16). Results are shown for an HAB0 of 2 mm.

Figure 10 shows results of selected fits to the data, which are also summarized in Fig. 11. In these fits, the value C for each run was constrained to the value determined from fits to the slopes shown in Fig. 8 for high-HABs, and n_e was allowed to vary independently of R_e.
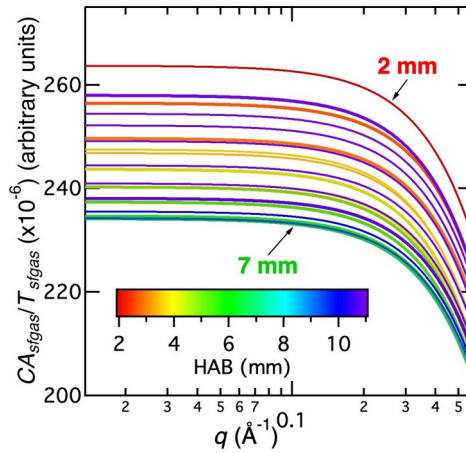
Figure 11. Gas-phase contributions to the signal for a range of HABs. Values of

$$CI_{sfgas}(q) = C \frac{A_{sfgas}(q, \text{HAB}\,x)}{T_{sfgas}(\text{HAB}\,x)}$$ were derived using fits of Eq. (15) to the data in Fig. 10 with

measured values of temperature. Lines are color coded by HAB as indicated by the color scale.

3.5 Contributions to the Measured Signal from Gas-Phase Species and Particles.

Rearranging Eq. (16) yields an expression for the contributions to the scattering from soot, i.e.,

$$CI_{soot}(q, \text{HAB}\,x) = \frac{S_{sfraw}(q, \text{HAB}\,x)}{\psi_{sf1}} - \frac{S_{nsraw}(q, \text{HAB}\,0)}{\psi_{ns1}} + C \frac{A_{nsgas}(q, \text{HAB}\,0)}{T_{nsgas}(\text{HAB}0)} - C \frac{A_{sfgas}(q, \text{HAB}\,x)}{T_{sfgas}(\text{HAB}\,x)},$$
$$(17)$$

where the second and third terms on the right-hand side are equivalent to subtracting the

instrument function, i.e.,

$$CI_{inst}(q) = \frac{S_{nsraw}(q)}{\psi_{ns1}} - C \frac{A_{nsgas}(q)}{T_{nsgas}} \quad , \tag{18}$$

which is independent of HAB and derived by rearranging Eq. (13). Figure 12a shows the

scattering profiles attributable to soot, i.e., values for CI_{soot} derived using Eq. (17). The signal

from soot increases with increasing HAB between 2 and 6 mm and then decreases with HAB.

Figure 12b shows the same data on a linear scale, highlighting the signal at q values larger than

0.1 Å^{-1} at HABs greater than ~3 mm. These results have been analyzed in detail in another

paper.[44] Figure 12a shows results using an HAB0 of 2 mm, and Fig. S4a presents results using an

HAB0 of 11 mm. Figure 12a is reproduced as Fig. S4b for comparison with Fig. S4a. In

principle, the inferred values of CI_{soot} should be independent of which HAB is used for HAB0,

assuming no soot or other anomalous scattering feature at the chosen HAB0. Differences

between the inferred soot signals using HAB0 of 2 mm and 11 mm are small, most pronounced

at small q, and vary from run to run, but are within the uncertainties of the retrieved soot signals.
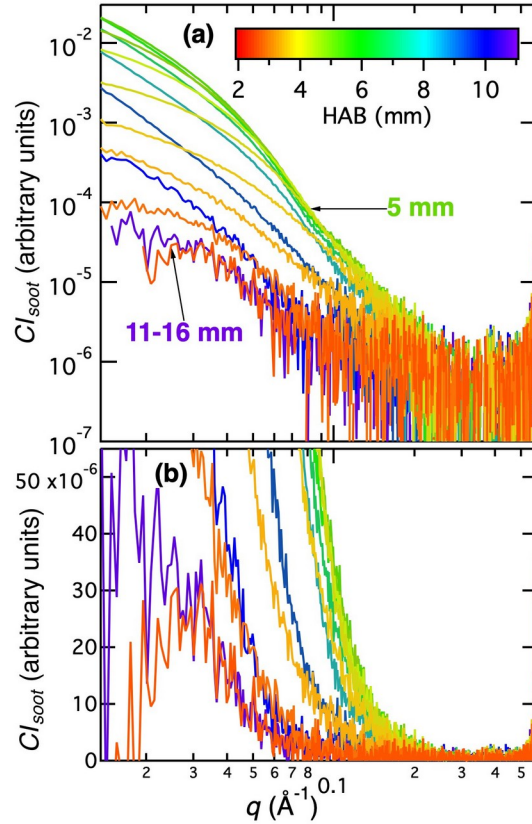
Figure 12. Soot contributions to the signal for a range of HABs. Values of $CI_{soot}(q)$ were derived using Eq. (17) and HAB0 of 2mm. Soot signal is shown on (a) a log scale and (b) a linear scale. Lines are color coded by HAB as indicated by the color scale in (a).

A direct comparison of CI_{inst}, CA_{gas}/T, and CI_{soot} is shown in Fig. 13 at two HABs. The normalized signal profiles are the same as the profiles shown in Fig. 9 at these HABs. The gas-phase signal profiles (CA_{gas}/T) are the same as those shown in Fig. 11 for these HABs. The soot signal profiles (CI_{soot}) reproduce the profiles from Fig. 12 at these HABs. The instrument function was calculated using Eq. (18).

At an HAB of 2.5 mm (Fig. 13a), the scattering from soot is negligible, and, at an HAB of 5 mm (Fig. 13b), the soot contribution is significant. The contribution to the scattering signal from

the gas-phase component is much smaller than that of CI_{inst}, particularly at small q, but there is a non-negligible contribution from the gas phase at large q.
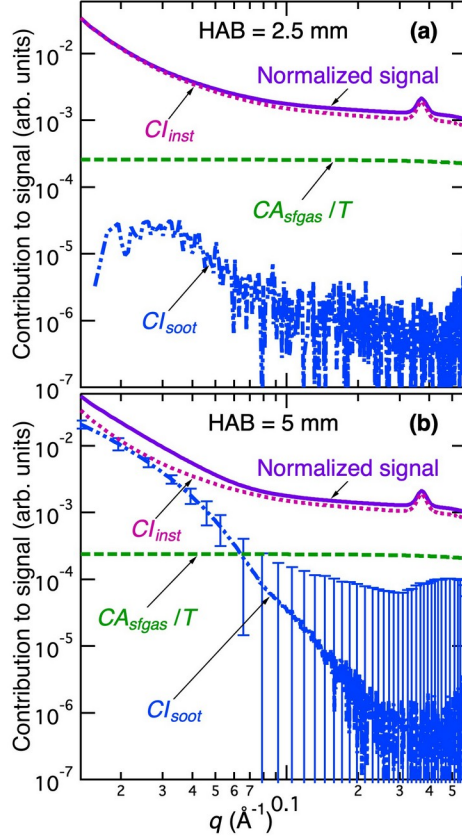

Figure 13. Relative contributions of CI_{inst}, CA_{sfgas}/T, and CI_{soot} to the scattering signal. Results are shown for HABs of (a) 2.5 mm and (b) 5 mm derived using an HAB0 of 2 mm. Solid purple lines show the normalized azimuthally integrated signal. Dotted pink lines show CI_{inst}. Dashed green lines show CA_{sfgas}, and dot-dashed blue lines show CI_{soot}. The error bars in (b) demonstrate the cumulative uncertainties of the soot signal described in Section C of the supplementary material. Every 20th error bar is displayed for clarity.

4. CONCLUSIONS

This study provides an approach for quantifying and addressing gas-phase temperature- and composition-dependent contributions to the SAXS signal in a flame or other high-temperature

reacting-flow system under a wide range of conditions. In Section 3.1, we compared the Guinier exponential form factor with the Debye form factor for gas-phase species and demonstrated that the Guinier functional form could be used to represent scattering from even small gas-phase species if slightly larger electronic radii of gyration (R_e) than predicted by the simple equilibrium atom-centric R_e model were used. We provided an expression to estimate these larger values of R_e given the number of electrons (n_e) in a molecular species. In Section 3.2, we demonstrated that scattering from gases in the flame is linearly proportional to inverse temperature. At a single q-value, the slope of the line given by a plot of scattering signal versus inverse temperature is related to the gas-phase composition, and the intercept is related to the temperature-independent instrument function. In Section 3.3, we verified that the Guinier exponential form factor can be used to fit the downward trend in slope as a function of q at higher q-values. In addition, we derived the gas-phase signal for the non-sooting regions to derive the instrument function by using the Guinier exponential form factor with the relationship between modified R_e and n_e (from Section 3.1) to fit the slopes derived as a function of q for the hydrogen flame and the non-sooting regions of the ethylene flame (from Section 3.2). These fits also allowed us to estimate an instrument calibration factor C. In Section 3.4, we used the Guinier exponential form factor and the value of C (from Section 3.3) to fit the high-q signal (minus the instrument function from Section 3.3) to estimate the gas-phase signal from the sooting flame. In Section 3.5, we isolated the soot signal by subtracting the instrument function (from Section 3.3) and the gas-phase signal (from Section 3.4) from the total normalized signal in the sooting flame. The soot signal is analyzed in detail in another paper.[44]

The steps for performing this analysis to distinguish the particle phase from the gas-phase background in a flame are as follows:

1. Subtract the SAXS signal (versus q) at a location in the flame where there are no particles from the SAXS signal (versus q) at all other locations in the flame.

2. At each value of q, plot the differenced signal as a function of inverse temperature, and fit the linear regions (where there is not soot) to determine the slope (e.g., Fig. 7).

3. Plot the slope as a function of q for a selected region, and fit the result using the Guinier function, i.e., Eq. (15), and the modified molecular electronic radius of gyration ($R_{e,\text{Modified}}$) as a function of the number of electrons (n_e), i.e., Eq. (10), with the instrument calibration factor C and n_e as adjustable parameters. The result of this fit gives and expression for

$$C\frac{A_{nsgas}(q)}{T_{nsgas}}.$$

4. Add this expression for $C\dfrac{A_{nsgas}(q)}{T_{nsgas}}$ to the differenced signals from Step 1.

5. Fit the regions for $q > {\sim}0.1$ of the profiles derived in Step 4 with the Guinier function, i.e, Eq. (15), using the value of C derived above with R_e and n_e as adjustable parameters. The result of this fit gives location-specific expressions for $C\dfrac{A_{sfgas}(q)}{T_{sfgas}}$.

6. Subtract these location- and temperature-dependent expressions for $C\dfrac{A_{sfgas}(q)}{T_{sfgas}}$ from the profiles derived in Step 4. Voilà; the result is the SAXS signal from soot!

This analysis demonstrates the value of complementary *in situ* measurements of temperature fields using CARS. These measurements enable the distinction between the temperature-dependent gas-phase scattering and the temperature-independent instrument function in regions where the composition does not change substantially. Decoupling these contributions to the scattering signal allows use of a physical model for accounting for gas-phase contributions in the

q-range of interest for studying particle inception without requiring a chemical kinetic model to estimate chemical composition and temperature.

Supporting Information.

GasPartSAXS_SM.docx provides descriptions of (A) previous work, (B) flame-length changes, (C) signal normalization and transmittance, (D) parameters used to quantify gas-phase contributions to the scattering, and (E) estimates of uncertainties.

NormSignal_E1_H1.xlsx contains normalized data and uncertainties for three datasets for Flame E1 and two datasets for Flame H1 and temperature measurements used in the analysis.
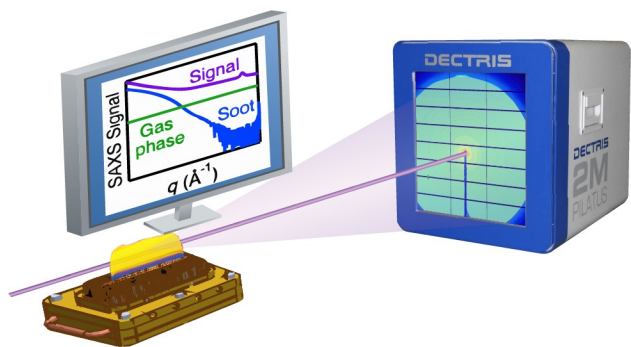
REFERENCES

(1)   Kammler, H. K.; Mädler, L.; Pratsinis, S. E., Flame synthesis of nanoparticles. *Chem. Eng. Technol.* **2001,** *24* (6), 583-596.
(2)   Kammler, H. K.; Beaucage, G.; Kohls, D. J.; Agashe, N.; Ilavsky, J., Monitoring simultaneously the growth of nanoparticles and aggregates by in situ ultra-small-angle x-ray scattering. *J. Appl. Phys.* **2005,** *97* (5), 054309.
(3)   Donnet, J.-B.; Bansal, R. C.; Wang, M.-J., *Carbon Black: Science and Technology*. 2nd ed.; Marcel Dekker, Inc.: New York, NY, 1993.
(4)   Teoh, W. Y.; Amal, R.; Mädler, L., Flame spray pyrolysis: An enabling technology for nanoparticles design and fabrication. *Nanoscale* **2010,** *2*, 1324-1347.
(5)   Strobel, R.; Pratsinis, S. E., Flame aerosol synthesis of smart nanostructured materials. *J. Mater. Chem.* **2007,** *17*, 4743-4756.
(6)   Beaucage, G.; Kammler, H. K.; Mueller, R.; Strobel, R.; Agashe, N.; Pratsinis, S. E.; Narayanan, T., Probing the dynamics of nanoparticle growth in a flame using synchrotron radiation. *Nat. Mater.* **2004,** *3* (6), 370-373.
(7)   Narayanan, T., High brilliance small-angle X-ray scattering applied to soft matter. *Curr. Opin. Colloid Interface Sci.* **2009,** *14*, 409-415.
(8)   McKibbin, S. R.; Yingman, S.; Balmes, O.; Meuller, B. O.; Tågerud, S.; Messing, M. E.; Portale, G.; Sztucki, M.; Deppert, K.; Samuelson, L., et al., In situ observation of synthesized nanoparticles in ultra-dilute aerosols via X-ray scattering. *Nano Res.* **2019,** *12* (1), 25-31.
(9)   Wang, H., Formation of nascent soot and other condensed-phase materials in flames. *Proc. Combust. Inst.* **2011,** *33*, 41-67.
(10)   Michelsen, H. A.; Colket, M. B.; Bengtsson, P.-E.; D'Anna, A.; Desgroux, P.; Haynes, B. S.; Miller, J. H.; Nathan, G. J.; Pitsch, H.; Wang, H., A review of terminology used to describe soot formation and evolution under combustion and pyrolytic conditions. *ACS Nano* **2020,** *14*, 12470-12490.
(11)   Michelsen, H. A., Probing soot formation, chemical and physical evolution, and oxidation: A review of in situ diagnostic techniques and needs. *Proc. Combust. Inst.* **2017,** *36* (1), 717-735.
(12)   Johansson, K. O.; El Gabaly, F.; Schrader, P. E.; Campbell, M. F.; Michelsen, H. A., Evolution of maturity levels of particle surface and bulk during soot growth and oxidation in a flame. *Aerosol Sci. Tech.* **2017,** *51* (12), 1333-1344.
(13)   Bras, W.; Koizumi, S.; Terrill, N. J., Beyond simple small-angle X-ray scattering: Developments in online complementary techniques and sample environments. *IUCrJ* **2014,** *1* (6), 478-491.

(14)   England, W. A., An *in situ* X-ray small angle scattering study of soot morphology in flames. *Combust. Sci. Technol.* **1986,** *46* (1-2), 83-93.

(15)   Mitchell, J. B. A.; Courbe, J.; Florescu-Mitchell, A. I.; di Stasio, S.; Weiss, T., Demonstration of soot particle resizing in an ethylene flame by small angle x-ray scattering. *J. Appl. Phys.* **2006,** *100* (12), 124918.

(16)   Sztucki, M.; Narayanan, T.; Beaucage, G., *In situ* study of aggregation of soot particles in an acetylene flame by small-angle x-ray scattering. *J. Appl. Phys.* **2007,** *101* (11), 114304.

(17)   Mitchell, J. B. A.; di Stasio, S.; LeGarrec, J. L.; Florescu-Mitchell, A. I., Synchrotron radiation studies of additives in combustion I: Water. *Nucl. Instrum. Meth. B* **2010,** *268* (9), 1486-1491.

(18)   Mitchell, J. B. A.; di Stasio, S.; LeGarrec, J. L.; Florescu-Mitchell, A. I.; Narayanan, T.; Sztucki, M., Small angle x-ray scattering study of flame soot nanoparticle aggregation and restructuring. *J. Appl. Phys.* **2009,** *105* (12), 124904.

(19)   di Stasio, S.; LeGarrec, J. L.; Mitchell, J. B. A., Synchrotron radiation studies of additives in combustion, II: Soot agglomerate microstructure change by alkali and alkaline-earth metal addition to a partially premixed flame. *Energy Fuels* **2011,** *25* (3), 916-925.

(20)   Hessler, J. P.; Seifert, S.; Winans, R. E.; Fletcher, T. H., Small-angle X-ray studies of soot inception and growth. *Faraday Discuss.* **2001,** *119* (1), 395-407.

(21)   Hessler, J. P.; Seifert, S.; Winans, R. E., Spatially resolved small-angle x-ray scattering studies of soot inception and growth. *Proc. Combust. Inst.* **2002,** *29* (2), 2743-2748.

(22)   di Stasio, S.; Mitchell, J. B. A.; LeGarrec, J. L.; Biennier, L.; Wulff, M., Synchrotron SAXS in situ identification of three different size modes for soot nanaoparticles in a diffusion flame. *Carbon* **2006,** *44*, 1267-1279.

(23)   Mitchell, J. B. A.; LeGarrec, J. L.; Saidani, G.; Lefeuvre, F.; di Stasio, S., Synchrotron Radiation Studies of Additives in Combustion, III: Ferrocene. *Energy Fuels* **2013,** *27* (8), 4891-4898.

(24)   Tang, X.; Wang, C.; Zhang, F.; Wang, Q.; Wang, J.; Seifert, S.; Winans, R. E., Effect of nickel acetylacetonate addition on soot inception and growth in an ethylene flame studied by using in situ small-angle X-ray scattering. *Combust. Flame* **2019,** *206*, 390-399.

(25)   Zhang, F.; Wang, C.; Han, W.; Zou, Y.; Wang, J.; Seifert, S.; Winans, R. E., Soot formation and growth with palladium acetylacetonate-toluene injection in ethylene base flames investigated by *in situ* synchrotron small-angle X-ray scattering. *Proc. Combust. Inst.* **2021,** *38*, 1859-1866.

(26)   Ossler, F.; Larsson, J., Measurements of the structures of nanoparticles in flames by *in situ* detection of scattered x-ray radiation. *J. Appl. Phys.* **2005,** *98* (11), 114317.

(27)   Ossler, F.; Canton, S. E.; Larsson, J., X-ray scattering studies of the generation of carbon nanoparticles in flames and their transition from gas phase to condensed phase. *Carbon* **2009,** *47* (15), 3498-3507.

(28)   Ossler, F.; Larsson, J., Exploring the formation of carbon-based molecules, clusters and particles by *in situ* detection of scattered X-ray radiation. *Chem. Phys. Lett.* **2004,** *387* (4-6), 367-371.

(29)   Gardner, C.; Greaves, G. N.; Hargrave, G. K.; Jarvis, S.; Wildman, P.; Meneau, F.; Bras, W.; Thomas, G., *In situ* measurements of soot formation in simple flames using small angle X-ray scattering. *Nucl. Instrum. Meth. B* **2005,** *238* (1-4), 334-339.

(30)   Ossler, F.; Vallenhag, L.; Canton, S. E.; Mitchell, J. B. A.; Le Garrec, J.-L.; Sztucki, M.; di Stasio, S., Dynamics of incipient carbon particle formation in a stabilized ethylene flame by *in situ* extended-small-angle- and wide-angle X-ray scattering. *Carbon* **2013,** *51*, 1-19.

(31)   di Stasio, S., Soot with 10^{13} cm^{-3} high concentration and 25 Å radius of gyration as detected by small-angle X-ray scattering in a premixed ethylene-air flame at sooting threshold. *J. Aerosol Sci.* **2017,** *110*, 11-24.

(32)   Vallenhag, L.; Canton, S. E.; Sondhauss, P.; Haase, D.; Ossler, F., A combined small- and wide-angle x-ray scattering detector for measurements on reactive systems. *Rev. Sci. Instrum.* **2011,** *82* (8), 083104.

(33)   Yon, J.; Ouf, F. X.; Hebert, D.; Mitchell, J. B. A.; Teuscher, N.; Le Garrec, J.-L.; Bescond, A.; Baumann, W.; Ourdani, D.; Bizien, T., et al., Investigation of soot oxidation by coupling LII, SAXS and scattering measurements. *Combust. Flame* **2018,** *190*, 441-453.

(34)   Campbell, M. F.; Bohlin, A.; Schrader, P. E.; Bambha, R. P.; Kliewer, C. J.; Johansson, K. O.; Michelsen, H. A., Design and characterization of a linear Hencken-type burner. *Rev. Sci. Instrum.* **2016,** *87* (11), 115114.

(35)   Hexemer, A.; Bras, W.; Glossinger, J.; Schaible, E.; Gann, E.; Kirian, R.; MacDowell, A.; Church, M.; Rude, B.; Padmore, H., A SAXS/WAXS/GISAXS beamline with multilayer monochromator. *J. Phys. Conf. Ser.* **2010,** *247*, 012007.

(36)   Englich, U.; Revesz, P.; Miller, W., A new beamstop for microfocus X-ray capillary beams. *Nucl. Instrum. Meth. A* **2011,** *649* (1), 101-103.

(37)   Kent, J. H.; Jander, H.; Wagner, H. G., Soot formation in a laminar diffusion flame. *Symp. (Int.) Comb.* **1981,** *18* (1), 1117-1126.

(38)   Kent, J. H.; Wagner, H. G., Soot measurements in laminar ethylene diffusion flames. *Combust. Flame* **1982,** *47*, 53-65.

(39)   Miller, J. H.; Elreedy, S.; Ahvazi, B.; Woldu, F.; Hassanzadeh, P., Tunable diode-laser measurement of carbon monoxide concentration and temperature in a laminar methane-air diffusion flame. *Appl. Opt.* **1993,** *32* (30), 6082-6089.

(40)   Ilavsky, J., Nika: software for two-dimensional data reduction. *J. Appl. Crystallogr.* **2012,** *45* (2), 324-328.

(41)   WaveMetrics *Igor Pro*, Lake Oswego, OR, USA.

(42)   Guinier, A.; Fournet, G., *Small-Angle Scattering of X-Rays*. John Wiley & Sons, Inc.: New York, 1955.

(43)   Ma, L.; Yong, H.; Geiser, J. D.; Carrascosa, A. M.; Goff, N.; Weber, P. M., Ultrafast x-ray and electron scattering of free molecules: A comparative evaluation. *Struct. Dyn.* **2020,** *7*, 034102.

(44)   Michelsen, H. A.; Campbell, M. F.; Johansson, K. O.; Tran, I. C.; Schrader, P. E.; Bambha, R. P.; Cenker, E.; Hammons, J. A.; Schaible, E.; Zhu, C., et al., Soot-Particle Core-Shell and Fractal Structures from Small-Angle X-Ray Scattering Measurements in a Flame. *Carbon* **2022**, Submitted.

(45)   Willmott, P., *An Introduction to Synchrotron Radiation*. 2nd ed.; Wiley: Hoboken, NJ, 2019.

(46)   Feigin, L. A.; Svergun, D. I., *Structure Analysis by Small-Angle X-Ray and Neutron Scattering*. Springer: New York, 1987.

(47)   Debye, P., Zerstreuung von Röntgenstrahlen. *Ann. Phys.* **1915,** *351* (6), 809-823.

(48)   Scardi, P.; Billings, S. J. L.; Neder, R.; Cervellino, A., Celebrating 100 years of the Debye scattering equation. *Acta Crystallogr. A* **2016,** *72*, 589-590.

(49)   Brown, P. J.; Fox, A. G.; Maslen, E. N.; O'Keefe, M. A.; Willis, T. M., Intensity of diffracted intensities. In *International Tables for Crystallography*, Prince, E., Ed. Wiley: Online, 2006; Vol. C, pp 554-595.

(50)   Hubbell, J. H.; Veigele, W. J.; Briggs, E. A.; Brown, R. T.; Cromer, D. T.; Howerton, R. J., Atomic form factors, incoherent scattering functions, and photon scattering cross sections. *J. Phys. Chem. Ref. Data* **1975,** *4* (3), 471-538.

(51)   Hubbell, J. H.; Veigele, W. J.; Briggs, E. A.; Brown, R. T.; Cromer, D. T.; Howerton, R. J., Erratum: Atomic form factors, incoherent scattering functions, and photon scattering cross sections. *J. Phys. Chem. Ref. Data* **1977,** *6* (2), 615-616.

(52)   Svergun, D. I.; Koch, M. H. J., Small-angle scattering studies of biological macromolecules in solution. *Rep. Prog. Phys.* **2003,** *66* (10), 1735-1782.

(53)   Vainio, U., Small-angle X-ray Scattering. In *X-Ray Diffraction: Modern Experimental Techniques*, Seeck, O. H.; Murphy, B. M., Eds. Pan Stanford Publishing: Singapore, 2015; pp 90-118.

TOC Graphic